Acta Materialia 225 (2022) 117564

Contents lists available at ScienceDirect

Acta Materialia

journal homepage: www.elsevier.com/locate/actamat

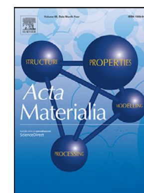

Full length article

Microscopic physical origin of polarization induced large tunneling electroresistance in tetragonal-phase $BiFeO_3$

Jing Wang[a,b,*], Yuanyuan Fan[a], Yan Song[b], Jialu Wu[b], Ruixue Zhu[c], Rongzhen Gao[a], Cancan Shao[a], Houbing Huang[a], Peng Gao[c], Ben Xu[b], Jing Ma[b], Jinxing Zhang[d], Ce-Wen Nan[b,1]

[a] Advanced Research Institute of Multidisciplinary Science, School of Materials Science and Engineering, Beijing Institute of Technology, Beijing 100081, China
[b] State Key Laboratory of New Ceramics and Fine Processing, School of Materials Science and Engineering, Tsinghua University, Beijing 100084, China
[c] International Center for Quantum Materials, Electron Microscopy Laboratory, School of Physics, Peking University, Beijing 100871, China
[d] Department of Physics, Beijing Normal University, Beijing 100875, China

A R T I C L E I N F O

Article history:
Received 15 August 2021
Revised 15 December 2021
Accepted 15 December 2021
Available online 18 December 2021

A B S T R A C T

Ferroelectric tunnel junctions have attracted intensive research interest due to the fundamental physics and potential applications in high-density data storage and neuromorphic computation. However, the intrinsic physical origin, especially at atomic scale, of polarization-controllable tunneling current is still controversial due to the degradation of ferroelectric polarization and the extrinsic conduction induced by defects or oxygen vacancies. Here, a large tunneling electroresistance effect of over 10,000% in a thick (~15 nm) tetragonal-phase $BiFeO_3$ thin film is observed, where a nanoscale point-contact geometry is delicately designed to reduce the extrinsic defect effects. By combining transmission electron microscopy and first-principles calculations, the atomic and electronic structures of $BiFeO_3$ tunneling layer are investigated. The corresponding results indicate the different charge transfer occurs at the top and bottom interface, which induces distinct tunneling barrier asymmetry when the polarization direction is opposite.
© 2021 Acta Materialia Inc. Published by Elsevier Ltd. All rights reserved.

1. Introduction

Polarization controllable tunneling behaviors in ferroelectric tunneling junctions (FTJs) [1–3] has attracted intensive research interest due to the applications for high-density integrated multi-state memories [4–7] and ultra-fast solid state neuromorphic synapse emulation [8,9]. To date, a lot of efforts have been taken to modulate the so-called tunneling electroresistance (TER) effect, such as introducing the asymmetric potential profile in metal/ferroelectric/metal (M_1/F/M_2) [1,10,11] or metal/ ferroelectric/semiconductor (M/F/S) junctions, inserting phase transition interlayer (e.g. doped manganites) [12–14], taking advantage of ionic controlled interface engineering [15] or utilizing two-dimensional ferroelectric tunneling barrier [10]. However, the intrinsic physical origin of polarization controlled ON/OFF states in FTJs is still obscure, especially at the atomic scale.

The challenge of exploring the intrinsic physical origin of polarization-modulated TER effect arises from the following. First, by using of a capacitor configuration, almost all FTJs require ultrathin (normally several unit cells) ferroelectric tunneling barrier [14,16,17]. Whereas, this requirement is contradictory to the ferroelectric degradation effect in the thin films with limited thickness [18], resulting in the extrinsic conduction mechanism, such as defects induced leakage current or oxygen vacancy induced resistive switching effect [19,20], dominant instead of the intrinsic one. Additionally, the large contact area between the metallic electrode and ferroelectric oxide surface will increase the transport area of carriers, which induces a large defects concentration and a large number of conduction filaments [21], resulting in low TER effect. To address these challenges, on the one hand, ferroelectric tunneling barrier with an intrinsic large polarization magnitude is needed to magnify the asymmetric effect of interfacial potential barrier [22,23]; on the other hand, it is highly desired to design a FTJ geometry allowing ferroelectric tunneling behaviors occur in thick thin films with robust polarization, which can effectively reduce the extrinsic defect effect.

Previous reports have demonstrated that tetragonal-phase $BiFeO_3$ (T-BFO) exhibits a large magnitude (150 $\mu C/cm^2$) of ferroelectric polarization [24,25], providing us a good candidate for ex-

* Corresponding author at: Advanced Research Institute of Multidisciplinary Science, School of Materials Science and Engineering, Beijing Institute of Technology, Beijing 100081, China.
E-mail address: jwang@bit.edu.cn (J. Wang).
[1] This author was an editor of the journal during the review period of the article.

https://doi.org/10.1016/j.actamat.2021.117564
1359-6454/© 2021 Acta Materialia Inc. Published by Elsevier Ltd. All rights reserved.

ploring the ferroelectric tunneling behavior. In this work, we investigate the local ferroelectric tunneling behaviors based on Pt/T-BFO/(La,Sr)MnO_3 (Pt/T-BFO/LSMO) junction by utilizing a point-contact geometry, where the large local electric field allows ferroelectric tunneling process occurs in thick thin films, and the small contact area between the nanoscale top electrode and ferroelectric film surface also shrinks the transport area for the tunneling carriers, effectively decreases the defects effect and thus enhances the TER effect. By combination of scanning transmission electron microscopy (STEM) and first-principles calculations, the modulation of potential barrier at the top and bottom interfaces by the opposite polarization is investigated, which explains the high and low conductance state and the large TER effect in this T-BFO based FTJ.

2. Experimental methods

T-BFO thin films with a ~15 nm thickness is grown on (001)-oriented $LaAlO_3$ (LAO) single-crystal substrate by a pulsed laser deposition (PLD) technique. LSMO thin film with a thickness of ~3 nm is deposited beforehand as the bottom electrode. The growth temperature for both T-BFO and LSMO is maintained at 680 °C, and the growth oxygen pressure is maintained under 0.2 mbar. During the thin-film growth, a KrF excimer laser with a wavelength of 248 nm, repetition rate of 5 Hz, and energy density of ~1.5 J/cm^2 is used. After the thin-film deposition, the specimens are slowly cooled down to room temperature with an oxygen pressure of 200 mbar and a cooling rate of 10°C/min.

The morphology, ferroelectric domains and *I-V* curves for BFO films are characterized by atomic force microscopy (AFM) system (Infinity Asylum Research AFM and Bruker AFM). The ferroelectric domain pattern and the polarization switching loops are characterized by the piezoresponse force microscopy (PFM) mode. *I-V* curves of T-BFO films are performed in ambient conditions by conducting-atomic force microscopy (c-AFM) mode. During PFM and c-AFM measurements, a commercial AFM tip with Pt/Ir-coated Si cantilever is used as a top electrode.

The crystalline structure of the epitaxial T-BFO thin film is characterized by X-ray diffraction (PANalytical X′Pert), which include $\theta-2\theta$ scan and RSM diffraction pattern around (002) LAO. Additionally, an aberration-corrected FEI Titan Themis G2 operated at 300 kV is used for atomic-structure analysis for the interfaces of BFO/LSMO/LAO junction, with sub-Angstrom spatial resolution. We determine the position of atoms in the atomically resolved HAADF image by simultaneously fitting two-dimensional Gaussian peaks, thus calculating the polarization. The TEM sample is prepared by traditional mechanical polishing and argon ion milling with PIPS^{TM} (Model 691, Gatan Inc.).

First-principles calculations are performed using VASP [26,27] with the generalized gradient approximation parameterized by Perdew et al. [28]. We construct a LSMO/T-BFO/Pt junction with five atomic layers of LSMO, nine of T-BFO and five of Pt. The in-plane lattice constant is fixed with the value of LAO ($a = b = 3.79$ Å). The internal coordinates of all the layers of T-BFO, two interfacial layers of LSMO and one interfacial layer of Pt are fully relaxed. The energy and force convergence criteria are 10^{-5} eV/atom and 0.03 eV/Å, respectively. By convergence test, Kohn-Sham single-particle wavefunctions are expanded in the plane wave basis set with an energy cutoff at 500 eV, and Monkhorst-Pack *k*-mesh of 3 × 3 × 1 is used for the FTJ models. A vacuum layer of 24 Å is adopted to prevent the artificial coupling between adjacent periodic images. The on-site Coulomb interactions of 3d states are treated within GGA+U approach with U_{eff} = 3 [29] and 4 eV [30] for Mn and Fe, respectively.

3. Results and discussion

Epitaxial T-BFO thin films are prepared on LAO substrate by using a PLD technique, where a LSMO bottom electrode with a thickness of ~3 nm is pre-grown for the electrical transport measurement. Fig. 1(a) shows AFM image of the film surface with atomic-scale terraces. Additionally, the crystalline structure of the thin film is characterized by X-ray diffraction (XRD), and the strong signal in Reciprocal Space Map (RSM) around LAO-(002) (Fig. 1(b)) indicates a good epitaxial feature of T-BFO thin film. The electron diffraction pattern (Fig. S1(a)) and the calculated c/a ratio of ~1.26 (Fig. S1(b)) further confirm the pure T-phase of the thin film, which is consistent with the previous observation [24,31–33]. Fig. 1(c) shows high-angle annular dark-field (HAADF)-STEM image for the BFO/LSMO hetero-structure, where the white arrow indicates the as-grown polarization orientation pointing from LSMO to BFO, and the yellow arrows describe the direction and magnitude of the polarization in each unit cell. Fig. 1(d) shows the average polarization magnitude within the orange box in Fig. 1(c), which demonstrates the large polarization magnitude of ~ 140 μC/cm^2 for T-BFO in the location away from the interface. Before we investigate the polarization modulated TER effect for T-BFO, the corresponding ferroelectric properties are characterized by PFM. The rectangular hysteresis loops with a phase variation of ~180° during the polarization switching in Fig. 1(e) indicates the robust ferroelectric properties of the T-BFO thin film. The distinction between positive and negative coercive fields arises from the asymmetric built-in fields at the top and bottom interfaces [34–36]. Further PFM phase images in Fig. S2 indicates the as-grown domain state is uniformly upward, which is also consistent with the polar mapping in STEM data in Fig. 1(c) and the previous reports [24,34]. Fig. 1(f) shows the box-in-box domain pattern, where the out-of-plane downward and upward poling field (±5 V) is applied on the scanning probe in a 3 × 3 μm^2 (bright color) and a 1 × 1 μm^2 (dark color) area, respectively. Such box-in-box domain pattern also indicates the fewer pining defects in the thin film.

In FTJs with perpendicular capacitor structures (see Fig. 2(a)), upward/ downward ferroelectric polarizations will induce positive/negative ('+'/'-') and negative/positive ('-'/'+') bound charges accumulating at top and bottom interfaces, respectively. The positive and negative bound charges will induce screening charges, e.g., electrons ('⊖') accumulating/depleting at the top Pt/BFO interface and holes ('⊕') accumulating/depleting at the bottom BFO/LSMO interface, respectively [37]. Such kind of field effect will induce distinct tunneling barriers for FTJs with opposite polarization states, and thus the corresponding different conductance states. To reduce the extrinsic effect (such as charged defects) on the ferroelectric tunneling process, a point-contact geometry, with a nanoscale top electrode, is delicately designed as shown in the schematics of Fig. 2(b). Before we investigate the ferroelectric tunneling behavior of T-BFO, a downward domain region is pre-poled utilizing the scanning probe with positive voltage of 5 V. Fig. 2(b) shows the typical current-voltage (*I-V*) hysteresis loops obtained from different locations of T-BFO thin film by c-AFM, where the FTJ exhibits high resistance state when the polarization is downward, while it dramatically changes to a low resistance state when the polarization is switched to upward by the positive sample bias. The difference of the switching voltage for ferroelectric polarization (0.6 V in Fig. 1(e)) and the resistance state (2.0 V in Fig. 2(b)) is consistent with that of other works [3,38,39]. Additionally, the contribution of charge defects can also be excluded from the following two points: First, due to a nanoscale Pt tip (contact radius: ~10 nm [40]) was used as the top electrode, the contact area between the top electrode and T-BFO surface was greatly decreased. Thus, the concentration of the possible charge defects during the electrical transport process can be largely reduced, as demonstrated by the

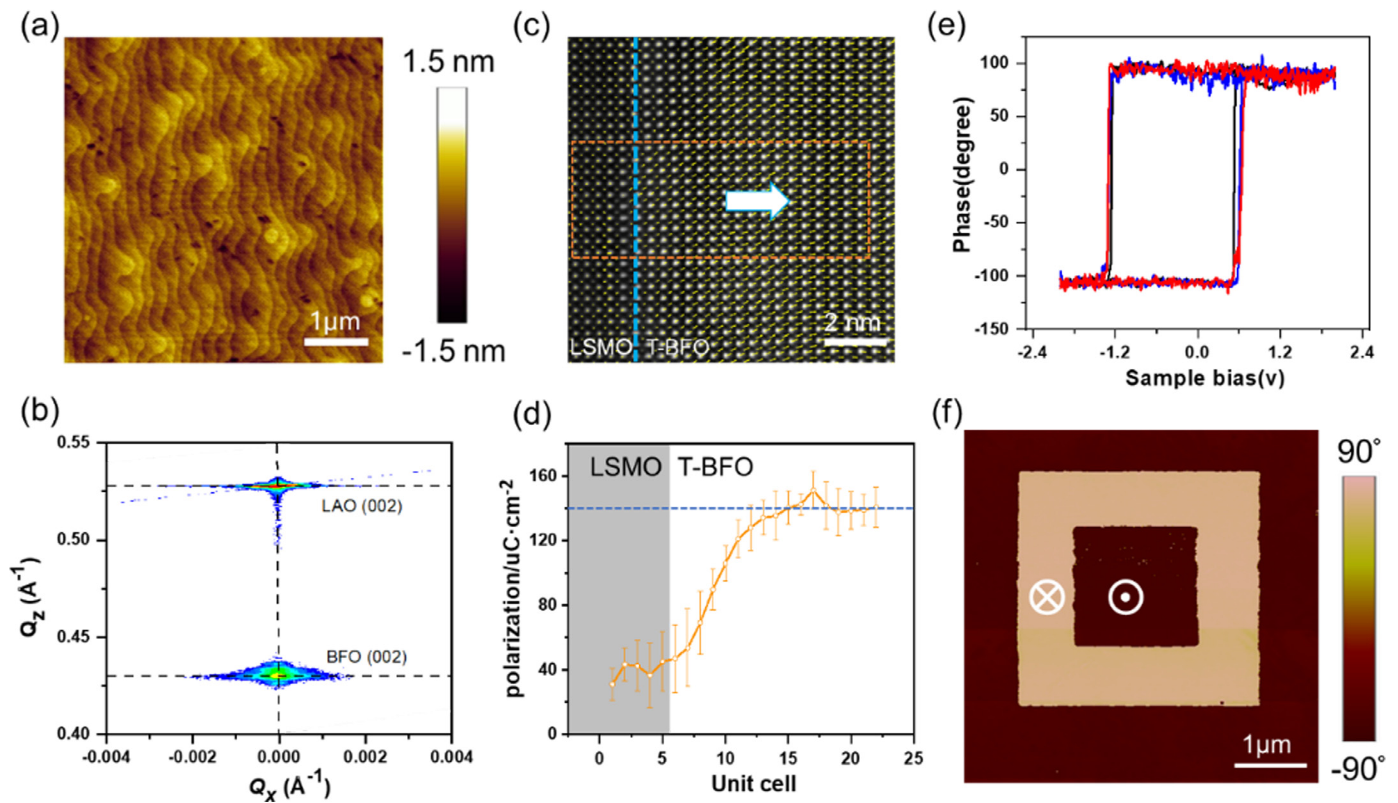

Fig. 1. High-quality T-BFO thin film and the corresponding ferroelectric properties. (a) Surface morphology of the (001)-oriented T-BFO film. (b) RSM pattern of T-BFO/LSMO/LAO heterostructure around (002)-LAO. (c) HAADF-STEM image and overlaid polar vectors of T-BFO/LSMO. Scale bar, 2 nm. (d) Polarization evolution along orange dashed line across BFO/LSMO interface. (e) PFM phase-voltage loops obtained from different locations of T-BFO surface. (f) Out-of-plane PFM phase image for a box-in-box domain pattern.

I-V curve in Fig. S3, where the *I-V* curve for the high resistance state (downward domain state) shows negligible current until an abrupt enhancement of the current occurs at the switching voltage. Second, the *I-V* curve shows a unidirectional feature in our work (Fig. S3), which is different from the *I-V* curve obtained in a Calcium-ion doped BFO [41], where the electrical transport is majorly controlled by the charged defects (e.g., oxygen vacancies), and a bidirectional feature is always observed for the *I-V* curve in that case. Since the tunneling current at low resistance state is over the limitation of the current amplifier, each *I-V* curve shows a platform when the current magnitude is above ~600 nA. In order to calculate the TER, the backward tunneling current is extracted from the fitting curves, as described by the dashed lines in Fig. 2(b). One can clearly see that the difference of the abrupt tunneling current with upward polarizations and the corresponding TER within the investigated voltage range (Fig. 2(c)) is very small, which indicate the homogeneous and intrinsic ferroelectric tunneling behavior observed in T-BFO thin film with point contact geometry. The maximum TER for this FTJ with ~15 nm ferroelectric tunneling barrier approaches to ~3 × 10,000%, which is nearly close to the case within ultrathin (~4.6 nm) T-BFO tunneling barrier [22].

The *I-V* curves with semi-logarithmic coordinate are also plotted as shown in Fig. 2(d–f), which further indicates the negligible current for the high-resistance state, which takes advantage of the point-contact geometry used in our work. To further analysis the conduction mechanism for the large conduction with an upward polarization state, the *I-V* curve obtained for the upward polarization state with multiple conduction mechanisms, including Thermionic emission (Schottkey emission) [42], Poole-Frenkel Emission [43], and Fowler-Nordheim tunneling [44], respectively, as shown in Fig. 2(g–i). Thus, we conclude that for the small sweeping voltage (0.8~1.5 V), the *I-V* curve is consistent with the Thermionic emission (Schottkey emission). While for the large sweeping voltage (1.5~1.9 V), the I-*V* curve can be described using Poole-Frenkel emission or Fowler-Nordheim tunneling model.

Before we investigate the significant role of polarization-dependent interfacial barriers on tunneling behaviors, the atomic stacking sequences of BFO/LSMO/LAO heterostructure are confirmed by STEM as shown in Fig. 3. From HAADF-STEM image of Fig. 3(a), the sharp LSMO/LAO and BFO/LSMO interfaces can be clearly observed, indicating a good epitaxial quality. The energy dispersive spectrometer (EDS) mapping images for La, Al and Mn demonstrates the termination of AlO_2-plane for LAO substate, and the atomic stacking sequence is LaO-AlO_2-(La,Sr)O-MnO_2 for LSMO/LAO interface and (La,Sr)O-MnO_2-BiO-FeO_2 for BFO/LSMO interface. This atomic stacking sequence is also illustrated in Fig. 3(b). One thing we need to notice is that this staking model has been also demonstrated to show an upward built-in bias for this junction, which results in the virgin domain state is upward [45,46], well consistent with the above PFM and TEM results.

According to the above experimental evidence of atomic staking sequences, first-principles calculations are performed to construct Pt/T-BFO/LSMO heterostructure and explore the corresponding charge transfer at the top and bottom interface, respectively. As shown in Fig. 4(a) and 4(b), the atomic structure of Pt/T-BFO/LSMO heterostructure with five atomic layers of LSMO, nine of T-BFO and five of Pt is constructed, where the polarization in BFO layer points to LSMO and Pt, respectively. In order to facilitate the analysis, we now define the alternative BiO-layer and FeO_2-layer to be layer-I (close to BFO/LSMO interface) to layer-IX (close to Pt/BFO interface), respectively. According to the first-principles results, charge transfer occurs both at BFO/LSMO and Pt/BFO in-

Fig. 2. Polarization-dependent TER effect in Pt/T-BFO/LSMO junction with a point-contact geometry. (a) Modulation of interfacial screening charges by opposite polarizations in Pt/BFO/LSMO junction. (b), (c) *I-V* curves and TER obtained from different data points in T-BFO thin film. (d–f) *I-V* curves plotted with a semi-logarithmic coordinate. (g–i) Conduction mechanism analysis for the large conduction with an upward polarization state. Data plotted in linear coordinates for Schottkey emission (g), Poole-Frenkel emission (h), and Fowler-Nordheim tunneling (i), respectively.

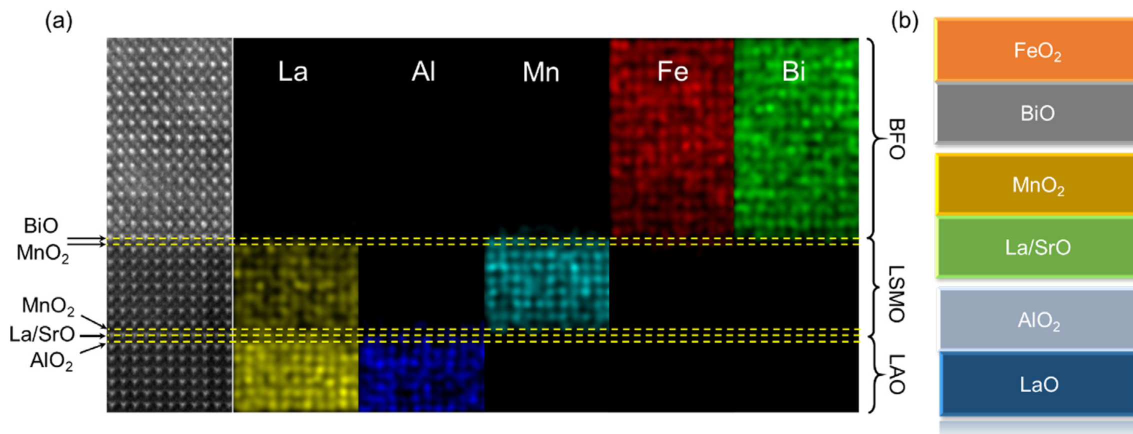

Fig. 3. Atomic stacking sequence for LSMO/LAO and T-BFO/LSMO interfaces. (a) HAADF and EDS images for the T-BFO/LSMO/LAO heterostructure. The arrangement for the EDS images (from left to the right): La, Al, Mn, Fe, Bi, and mixed elements. (b) Schematic diagram of the stacking sequence for the heterostructure.

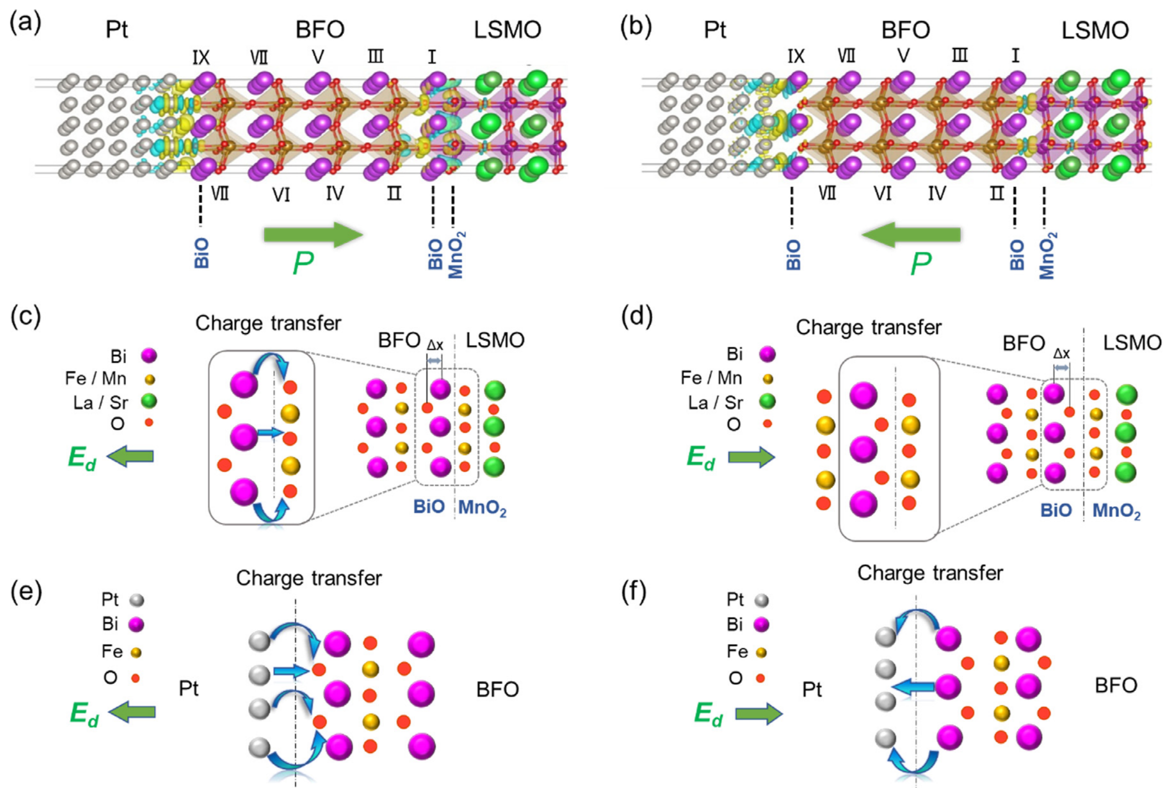

Fig. 4. First-principles calculation of charge density for Pt/T-BFO/LSMO junction with opposite polarization state. (a), (b) Charge density differences for Pt/T-BFO/LSMO junction with downward and upward polarization state, respectively. Yellow (blue) area represents the net gain (loss) of electrons. (c)–(f) Schematics for charge transfer at BFO/LSMO (c, d) and Pt/BFO (e, f) interface when the polarization points to LSMO (c, e) and Pt (d, f), respectively.

terfaces, as indicated by the blue (lost charges) and yellow (gain charges) area in Fig. 4(a) and 4(b), respectively. To fully understand the charge transfer at the top and bottom interfaces with the opposite polarization directions, schematic diagrams are shown in Fig. 4(c)–4(f), respectively. When the polarization of BFO points to LSMO (Fig. 4(a)), the charges transfer from Bi atoms in layer-I BiO layer to O atoms in MnO_2 layer at the bottom BFO/LSMO interface (Fig. 4(c)), while which occurs between Pt atoms and O atoms in layer-IX BiO layer at the top Pt/BFO interface. When the polarization of BFO points to Pt, electronic reconstruction occurs for O atoms in layer-I BiO layer at the bottom BFO/LSMO interface, while charges transfer occurs between Pt and layer-IX Bi atoms and O atoms at the top Pt/BFO interface.

To quantitative analysis of the polarization modulation of interfacial potential barrier, the energy level shift for the top of the valence band (the highest occupied energy state) and the bottom of the conduction band (the lowest unoccupied energy state) is discussed, which is based on the calculated density of states (DOSs) for the alternative BiO- and FeO_2-layers, as shown Fig. 5. As expected, the electronic states for BFO layers close to the top and bottom interface changes significantly, while that of the middle-layer BFO show negligible variation. The detailed analysis for the evolution of the energy level for each alternative BiO- and FeO_2-layer is illustrated as following. When the polarization points to LSMO (Fig. 5(a)), layer-1 BiO keeps semiconductor, but the bottom of the conduction band shifts close to the Fermi level (E_F) and the top of the valence band shifts away from E_F. This amplitude of the energy-level shift gradually decreases for the consequent FeO_2- (layer-II) and BiO- (layer-III) layer, and which keeps constant for the intermediate FeO_2- and BiO-layers (layer IV–VI). For BFO layers close to Pt/BFO interface, the energy-level shift shows the opposite trending, e.g., the bottom of the conduction band shifts away from E_F and the top of the valence band shifts close to E_F, as shown in the DOSs for VII and VIII layers. At Pt/BFO interface, layer-IX BiO changes to metallic state due to the interaction between electrons of O p-orbitals and Bi p-orbitals. Intriguingly, when the polarization is opposite, e.g., points to Pt electrode (Fig. 5(b)), the energy level shifts with the reversed trends. For layer-I BiO, the top of the valence band shifts close to E_F, which results in the electronic structure transforms to metallic state. This amplitude of energy-level shift decreases for the consequent FeO_2- (layer-II) and BiO-layer (layer-III), and which keeps constant for the middle (IV–VI) atomic layers. For BFO layers (layer-VII and VIII) close to Pt/BFO interface, the bottom of the conduction band shifts close to E_F and the top of the valence band shifts away from E_F. For layer-IX BiO, it transforms to metallic state due to the reconstruction between electrons of O p-orbitals and Bi p-orbitals.

To have a deep understanding of the high and low conductance states of FTJs with opposite polarization orientations, energy band diagram (Fig. 6) is drawn according to the above analysis for energy-level shift based on first-principles calculations. Fig. 6(a) schematically shows the energy band diagram of isolated Pt, BFO and LSMO layers. The work function for Pt and LSMO is 5.6 eV [47] and 4.8 eV [48], respectively. The band gap and electron affinity for BFO are 2.8 eV and 3.3 eV [49], respectively. Thus, the work function for BFO is ~4.7 eV. Fig. 6(b) shows the combined energy band diagram for the tunneling junction without considering the contribution from the polarization, where we can see a Schottky barrier with a barrier height of 2.3 eV forms at Pt/BFO interface. Now, we turn to discuss the modulation of interfacial potential barriers by the polarization. The quantitative analysis of the polarization control of the variation for barrier height at both top and bottom interfaces are highlighted in Fig. 6(c) and (d), where the changeable value of the barrier height is deduced from the shift

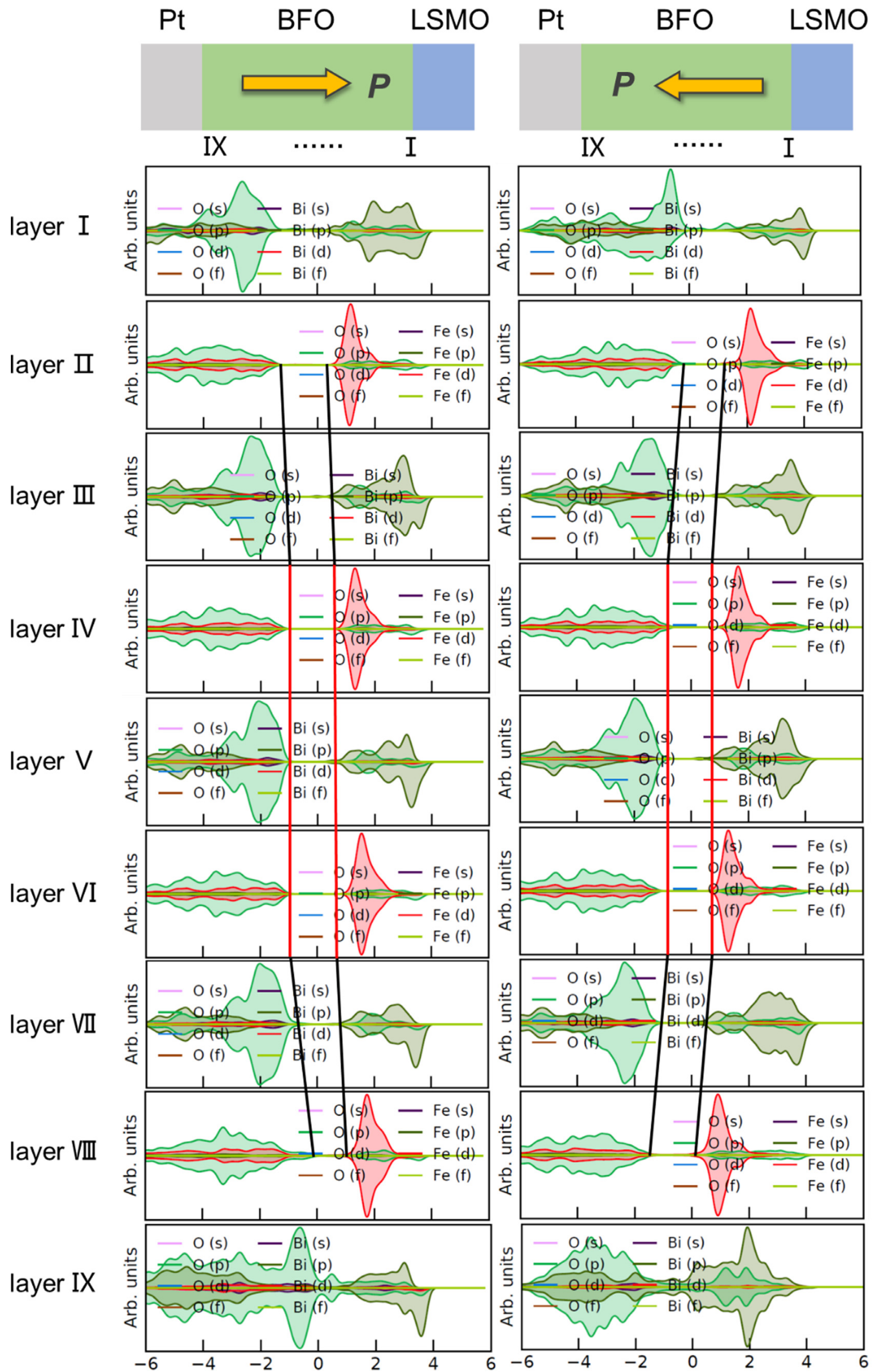

Fig. 5. Layer-resolved DOSs for T-BFO in Pt/T-BFO/LSMO heterostructure as a function of energy level. Layer-I BiO is close to BFO/LSMO interface, and layer-IX FeO_2 is close to Pt/BFO interface. (a) Layer-resolved DOSs for BFO with downward polarization state. (b) Layer-resolved DOSs for BFO with upward polarization state. Black and red lines are guide to the eyes to indicate the energy level shift. The Fermi level is set to zero.

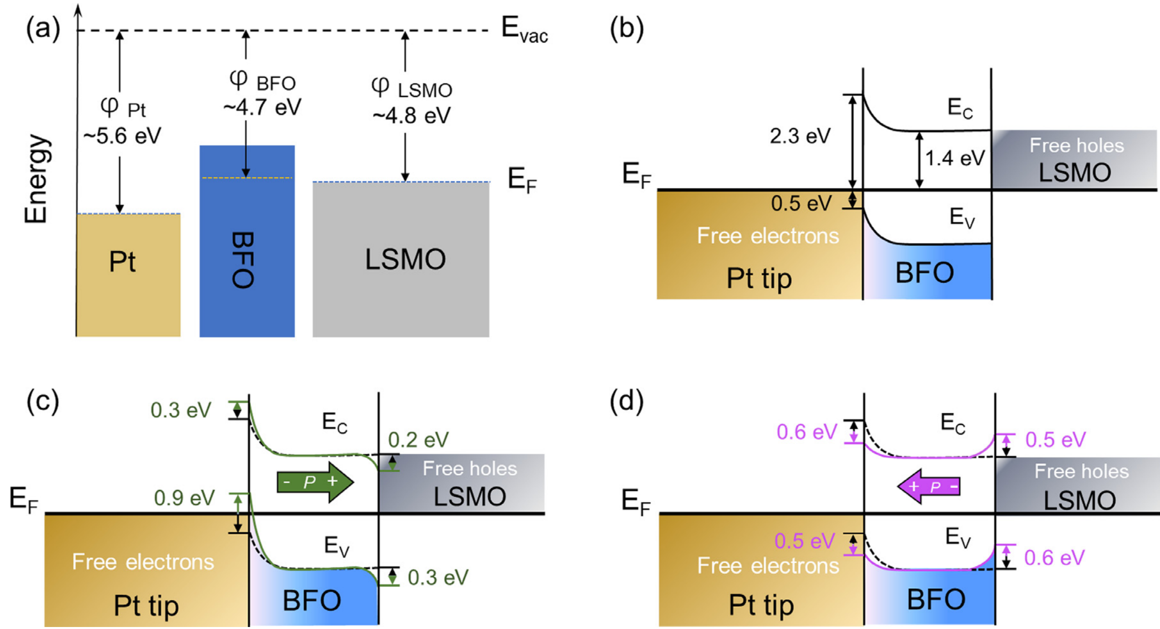

Fig. 6. Energy band diagram for Pt/T-BFO/LSMO junction with opposite polarization states. (a) Energy band diagram for isolated Pt, T-BFO and LSMO, where φ_{PT}, φ_{LSMO}, and φ_{BFO} is the work function of Pt, LSMO and T-BFO. E_{vac} and E_F represent the vacuum energy level and the Fermi level, respectively. (b) Energy band diagram for Pt/T-BFO/LSMO junction without considering the polarization contribution. (c, d) Energy band diagram for Pt/T-BFO/LSMO junction with downward and upward polarization state, respectively.

between the bottom of conduction band and the top of valence band for BFO layer in Fig. 5, and the evolution of the band bending is highlighted by black (indicating energy level with shift) and red lines (indicating energy level without shift) in Fig. 5. When the ferroelectric polarization of BFO thin film is downward (pointing to LSMO) as shown in Fig. 6(c), the bottom of the conduction band at Pt/BFO interface bends upward with additional 0.3 eV and the top of the valance band at this interface bends upward with additional 0.9 eV according to the energy-level shift between layer VIII and VI in Fig. 5(a). For BFO/LSMO interface, the bottom of the conduction band bends downward with 0.2 eV, and the top of the valence band bends downward with 0.3 eV, consulting the energy-level shift between layer II and IV in Fig. 5(a). While when the ferroelectric polarization of BFO film is upward (pointing to Pt electrode) as shown in Fig. 6(d), the upward band bending for the bottom (top) of the conduction (valence) band degrades with 0.6 eV (0.5 eV) at Pt/BFO interface, and the counterparts of the BFO/LSMO interface bends upward with 0.5 eV (0.6 eV) according to the energy-level shift (Fig. 5(b)) between layer VIII and VI for Pt/BFO interface and layer II and IV for BFO/LSMO interface, respectively. The above analysis for energy band bending with opposite polarization directions indicates that the downward polarization state increases the interfacial barrier height for both electrons (from Pt) and holes (from LSMO), while the upward polarization state decreases the interfacial barrier height both for the above two kinds of carriers, which well explains the high and low resistance states with downward and upward polarization state, respectively.

Based on the above band bending of the energy level for T-BFO obtained from first-principles calculations, the potential barriers (φ_1 and φ_2) of the top and bottom interfaces of the FJT under opposite polarization states can be estimated: when the polarization is downward (high resistance state), φ_1=2.6 eV, φ_2=1.2 eV, thus the average barrier for the downward polarization sate is $\bar{\varphi}_{\downarrow} = \frac{\varphi_1+\varphi_2}{2} = 1.9\,\text{eV}$; when the polarization is upward (low resistance state), $\varphi_1 = 1.7$ eV, $\varphi_2 = 1.9$ eV and thus the average barrier for the downward polarization sate is $\bar{\varphi}_{\uparrow} = \frac{\varphi_1+\varphi_2}{2} = 1.8\,\text{eV}$. According to the following approximation of TER [2]:

$$TER \approx \exp\left[\frac{\sqrt{2m}}{\hbar}\frac{\delta\varphi}{\sqrt{\bar{\varphi}}}d\right] \tag{1}$$

where $m = m_0$ (the free electron mass), $\hbar$ is the Planck constant, $\bar{\varphi} = \frac{\bar{\varphi}_{\downarrow}+\bar{\varphi}_{\uparrow}}{2} = 1.85\,\text{eV}$, $\delta\varphi = \bar{\varphi}_{\downarrow} - \bar{\varphi}_{\uparrow} = 0.1\,\text{eV}$ and $d = 15$ nm. Thus, the calculated TER is ~28,100%, which is approximately equal to the experimental result of ~30,000% obtained by the *I-V* curves in Fig. 2(b) and 2(c).

4. Conclusion

In summary, the ferroelectric tunneling behavior across a thick (~15 nm) T-BFO thin film based on a pint-contact geometry is investigated, where a large TER of ~28,100% is observed. First-principles calculations demonstrate that the polarization-mediated electronic reconstruction at the interfaces modulates the potential barrier and thus the electron tunneling magnitude. This study provides us a deep understanding of the microscopic physical origin of polarization induced TER effect, paving the way for designing new generation of electronic devices with ultrahigh performance.

Declaration of Competing Interest

The authors declare that they have no known competing financial interests or personal relationships that could have appeared to influence the work reported in this paper.

Acknowledgment

This work is supported by National Natural Science Foundation of China under Grant Nos. 12004036 and 11974052, and Beijing Institute of Technology Research Fund Program for Young Scholars. We are also grateful to Analysis & Testing Center at BIT.

Supplementary materials

Supplementary material associated with this article can be found, in the online version, at doi:10.1016/j.actamat.2021.117564.

References

[1] M.Y. Zhuravlev, R.F. Sabirianov, S.S. Jaswal, E.Y. Tsymbal, Giant electroresistance in ferroelectric tunnel junctions, Phys. Rev. Lett. 94 (2005) 246802.
[2] A. Gruverman, D. Wu, H. Lu, Y. Wang, H.W. Jang, C.M. Folkman, M.Y. Zhuravlev, D. Felker, M. Rzchowski, C.B. Eom, E.Y. Tsymbal, Tunneling electroresistance effect in ferroelectric tunnel junctions at the nanoscale, Nano Lett. 9 (2009) 3539–3543.
[3] Z. Wen, C. Li, D. Wu, A.D. Li, N.B. Ming, Ferroelectric-field-effect-enhanced electroresistance in metal/ferroelectric/semiconductor tunnel junctions, Nat. Mater. 12 (2013) 617–621.
[4] V. Garcia, M. Bibes, L. Bocher, S. Valencia, F. Kronast, A. Crassous, X. Moya, S. Enouz-Vedrenne, A. Gloter, D. Imhoff, C. Deranlot, N.D. Mathur, S. Fusil, K. Bouzehouane, A. Barthélémy, Ferroelectric control of spin polarization, Science 327 (2010) 1106–1110.
[5] D. Pantel, S. Goetze, D. Hesse, M. Alexe, Reversible electrical switching of spin polarization in multiferroic tunnel junctions, Nat. Mater. 11 (2012) 289–293.
[6] M. Gajek, M. Bibes, S. Fusil, K. Bouzehouane, J. Fontcuberta, A. Barthélémy, A. Fert, Tunnel junctions with multiferroic barriers, Nat. Mater. 6 (2007) 296–302.
[7] C. Ma, Z. Luo, W. Huang, L. Zhao, Q. Chen, Y. Lin, X. Liu, Z. Chen, C. Liu, H. Sun, X. Jin, Y. Yin, X. Li, Sub-nanosecond memristor based on ferroelectric tunnel junction, Nat. Commun. 11 (2020) 1439.
[8] S. Boyn, J. Grollier, G. Lecerf, B. Xu, N. Locatelli, S. Fusil, S. Girod, C. Carrétéro, K. Garcia, S. Xavier, J. Tomas, L. Bellaiche, M. Bibes, A. Barthélémy, S. Saïghi, V. Garcia, Learning through ferroelectric domain dynamics in solid-state synapses, Nat. Commun. 8 (2017) 14736.
[9] J. Li, C. Ge, J. Du, C. Wang, G. Yang, K. Jin, Reproducible ultrathin ferroelectric domain switching for high-performance neuromorphic computing, Adv. Mater. 32 (2020) 1905764.
[10] L. Kang, P. Jiang, N. Cao, H. Hao, X. Zheng, L. Zhang, Z. Zeng, Realizing giant tunneling electroresistance in two-dimensional graphene/BiP ferroelectric tunnel junction, Nanoscale 11 (2019) 16837–16843.
[11] S. Boyn, V. Garcia, S. Fusil, C. Carrétéro, K. Garcia, S. Xavier, S. Collin, C. Deranlot, M. Bibes, A. Barthélémy, Engineering ferroelectric tunnel junctions through potential profile shaping, APL Mater. 3 (2015) 061101.
[12] G. Radaelli, D. Gutiérrez, M. Qian, I. Fina, F. Sánchez, L. Baldrati, J. Heidler, C. Piamonteze, R. Bertacco, J. Fontcuberta, Strain-controlled responsiveness of slave half-doped manganite $La_{0.5}Sr_{0.5}MnO_3$ layers inserted in $BaTiO_3$ ferroelectric tunnel junctions, Adv. Electron. Mater. 2 (2016) 1600368.
[13] L. Jiang, W.S. Choi, H. Jeen, S. Dong, Y. Kim, M.G. Han, Y. Zhu, S.V. Kalinin, E. Dagotto, T. Egami, H.N. Lee, Tunneling electroresistance induced by interfacial phase transitions in ultrathin oxide heterostructures, Nano Lett. 13 (2013) 5837–5843.
[14] Y.W. Yin, J.D. Burton, Y.M. Kim, A.Y. Borisevich, S.J. Pennycook, S.M. Yang, T.W. Noh, A. Gruverman, G.X. Li, E.Y. Tsymbal, Q. Li, Enhanced tunnelling electroresistance effect due to a ferroelectrically induced phase transition at a magnetic complex oxide interface, Nat. Mater. 12 (2013) 397–402.
[15] J. Li, N. Li, C. Ge, H. Huang, Y. Sun, P. Gao, M. He, C. Wang, G. Yang, K. Jin, Giant electroresistance in ferroionic tunnel junctions, iScience 16 (2019) 368–377.
[16] Z. Wen, D. Wu, Ferroelectric tunnel junctions: modulations on the potential barrier, Adv. Mater. 32 (2019) 1904123.
[17] Z. Xi, J. Ruan, C. Li, C. Zheng, Z. Wen, J. Dai, A. Li, D. Wu, Giant tunnelling electroresistance in metal/ferroelectric/semiconductor tunnel junctions by engineering the Schottky barrier, Nat. Commun. 8 (2017) 15217.
[18] G. Pacchioni, S. Valeri, Oxide Ultrathin Films: Science and Technology, John Wiley & Sons, 2012.
[19] E.Y. Tsymbal, A. Gruverman, V. Garcia, M. Bibes, A. Barthélémy, Ferroelectric and multiferroic tunnel junctions, MRS Bull. 37 (2012) 138–143.
[20] Z. Wen, L. You, J. Wang, A. Li, D. Wu, Temperature-dependent tunneling electroresistance in $Pt/BaTiO_3/SrRuO_3$ ferroelectric tunnel junctions, Appl. Phys. Lett. 103 (2013) 132913.
[21] Y. Yin, Q. Li, A review on all-perovskite multiferroic tunnel junctions, J. Mater. 3 (2017) 245–254.
[22] H. Yamada, V. Garcia, S. Fusil, S. Boyn, M. Marinova, A. Gloter, S. Xavier, J. Grollier, E. Jacquet, C. Carrétéro, C. Deranlot, M. Bibes, A. Barthélémy, Giant Electroresistance of super-tetragonal $BiFeO_3$-based ferroelectric tunnel junctions, ACS Nano 7 (2013) 5385–5390.
[23] A. Sokolov, O. Bak, H. Lu, S. Li, E.Y. Tsymbal, A. Gruverman, Effect of epitaxial strain on tunneling electroresistance in ferroelectric tunnel junctions, Nanotechnology 26 (2015) 305202.
[24] J.X. Zhang, Q. He, M. Trassin, W. Luo, D. Yi, M.D. Rossell, P. Yu, L. You, C.H. Wang, C.Y. Kuo, J.T. Heron, R.J. Zeches, H.J. Lin, A. Tanaka, C.T. Chen, L.H. Tjeng, Y.H. Chu, R. Ramesh, Microscopic origin of the giant ferroelectric polarization in tetragonal-like $BiFeO_3$, Phys. Rev. Lett. 107 (2011) 147602.
[25] Y. Zhang, F. Xue, Z. Chen, J.M. Liu, L.Q. Chen, Presence of a purely tetragonal phase in ultrathin $BiFeO_3$ films: thermodynamics and phase-field simulations, Acta Mater. 183 (2020) 110–117.
[26] G. Kresse, J. Furthmüller, Efficient Iterative schemes for Ab initio total-energy calculations using a plane-wave basis set, Phys. Rev. B 54 (1996) 11169.
[27] G. Kresse, D. Joubert, From ultrasoft pseudopotentials to the projector augmented-wave method, Phys. Rev. B 59 (1999) 1758–1775.
[28] J.P. Perdew, K. Burke, M. Ernzerhof, Generalized gradient approximation made simple, Phys. Rev. Lett. 77 (1996) 3865–3868.
[29] X. Chen, S. Zhang, B. Liu, F. Hu, B. Shen, J. Sun, Theoretical investigation of magnetic anisotropy at the $La_{0.5}Sr_{0.5}MnO_3/LaCoO_{2.5}$ interface, Phys. Rev. B 100 (2019) 144413.
[30] H. Dong, C. Chen, S. Wang, W. Duan, J. Li, Elastic properties of tetragonal $BiFeO_3$ from first-principles calculations, Appl. Phys. Lett. 102 (2013) 182905.
[31] A.R. Damodaran, C.W. Liang, Q. He, C.Y. Peng, L. Chang, Y.H. Chu, L.W. Martin, Nanoscale structure and mechanism for enhanced electromechanical response of highly-strained $BiFeO_3$ thin films, Adv. Mater. 23 (2011) 3170–3175.
[32] C. Chen, C. Wang, X. Cai, C. Xu, C. Li, J. Zhou, Z. Luo, Z. Fan, M. Qin, M. Zeng, X. Lu, X. Gao, U. Kentsch, P. Yang, G. Zhou, N. Wang, Y. Zhu, S. Zhou, D. Chen, J.M. Liu, Controllable defect driven symmetry change and domain structure evolution in $BiFeO_3$ with enhanced tetragonality, Nanoscale 11 (2019) 8110–8118.
[33] R.J. Zeches, M.D. Rossell, J.X. Zhang, A.J. Hatt, Q. He, C.H. Yang, A. Kumar, C.H. Wang, A. Melville, C. Adamo, G. Sheng, Y.H. Chu, J.F. Ihlefeld, R. Erni, C. Ederer, V. Gopalan, L.Q. Chen, D.G. Schlom, N.A. Spaldin, L.W. Martin, R. Ramesh, A strain-driven morphotropic phase boundary in $BiFeO_3$, Science 326 (2009) 977–980.
[34] P. Yu, W. Luo, D. Yi, J.X. Zhang, M.D. Rossell, C.H. Yang, L. You, G. Singh-Bhalla, S.Y. Yang, Q. He, Q.M. Ramasse, R. Erni, L.W. Martin, Y.H. Chu, S.T. Pantelides, S.J. Pennycook, R. Ramesh, Interface control of bulk ferroelectric polarization, in: Proceedings of the National Academy of Sciences of the United States of America, 109, 2012, pp. 9710–9715.
[35] W. Geng, X. Tian, Y. Jiang, Y. Zhu, Y. Tang, Y. Wang, M. Zou, Y. Feng, B. Wu, W. Hu, X.L. Ma, Unveiling the pinning behavior of charged domain walls in $BiFeO_3$ thin films via vacancy defects, Acta Mater. 186 (2020) 68–76.
[36] M. Han, Y. Tang, Y. Wang, Y. Zhu, J. Ma, W. Geng, Y. Feng, M. Zou, N. Zhang, X.L. Ma, Charged domain wall modulation of resistive switching with large ON/OFF ratios in high density $BiFeO_3$ nano-islands, Acta Mater. 187 (2020) 12–18.
[37] Y. Tian, L. Wei, Q. Zhang, H. Huang, Y. Zhang, H. Zhou, F. Ma, L. Gu, S. Meng, L.Q. Chen, C.W. Nan, J.X. Zhang, Water printing of ferroelectric polarization, Nat. Commun. 9 (2018) 3809.
[38] Z. Xi, C. Zheng, Z. Wen, Nondestructive readout complementary resistive switches based on ferroelectric tunnel junctions, ACS Appl. Mater. Interfaces 10 (2018) 6024–6030.
[39] H. Fan, Z. Fan, P. Li, F. Zhang, G. Tian, J. Yao, Z. Li, X. Song, D. Chen, B. Han, M. Zeng, S. Wu, Z. Zhang, M. Qin, X. Lu, J. Gao, Z. Lu, Z. Zhang, J. Dai, X. Gao, J.M. Liu, Large electroresistance and tunable photovoltaic properties of ferroelectric nanoscale capacitors based on ultrathin super-tetragonal $BiFeO_3$ films, J. Mater. Chem. C 5 (2017) 3323–3329.
[40] M.M. Yang, D.J. Kim, M. Alexe, Flexo-photovoltaic effect, Science 360 (2018) 904.
[41] C.H. Yang, J. Seidel, S.Y. Kim, P.B. Rossen, P. Yu, M. Gajek, Y.H. Chu, L.W. Martin, M.B. Holcomb, Q. He, P. Maksymovych, N. Balke, S.V. Kalinin, A.P. Baddorf, S.R. Basu, M.L. Scullin, R. Ramesh, Electric modulation of conduction in multiferroic Ca-doped $BiFeO_3$ films, Nat. Mater. 8 (2009) 485–493.
[42] J. Seidel, P. Maksymovych, Y. Batra, A. Katan, S.Y. Yang, Q. He, A.P. Baddorf, S.V. Kalinin, C.H. Yang, J.C. Yang, Y.H. Chu, E.K.H. Salje, H. Wormeester, M. Salmeron, R. Ramesh, Domain wall conductivity in La-doped $BiFeO_3$, Phys. Rev. Lett. 105 (2010) 197603.
[43] S. Farokhipoor, B. Noheda, Conduction through 71° domain walls in $BiFeO_3$ thin films, Phys. Rev. Lett. 107 (2011) 127601.
[44] P. Maksymovych, S. Jesse, P. Yu, R. Ramesh, A.P. Baddorf, S.V. Kalinin, Polarization control of electron tunneling into ferroelectric surfaces, Science 324 (2009) 1421–1425.
[45] M. Chen, J. Wang, R. Zhu, Y. Sun, Q. Zhang, J. Ma, Y. Wang, L. Gu, P. Gao, J. Ma, C.W. Nan, Stabilization of ferroelastic charged domain walls in self-assembled $BiFeO_3$ nanoislands, J. Appl. Phys. 128 (2020) 124103.
[46] D. Yi, P. Yu, Y.C. Chen, H.H. Lee, Q. He, Y.H. Chu, R. Ramesh, Tailoring magnetoelectric coupling in $BiFeO_3/La_{0.7}Sr_{0.3}MnO_3$ heterostructure through the interface engineering, Adv. Mater. 31 (2019) 1806335.
[47] F. Yan, G. Chen, L. Lu, J.E. Spanier, Dynamics of photogenerated surface charge on $BiFeO_3$ films, ACS Nano 6 (2012) 2353–2360.
[48] M. Minohara, R. Yasuhara, H. Kumigashira, M. Oshima, Termination layer dependence of Schottky barrier height for $La_{0.6}Sr_{0.4}MnO_3$/Nb:$SrTiO_3$ heterojunctions, Phys. Rev. B 81 (2010) 235322.
[49] H. Yang, H.M. Luo, H. Wang, I.O. Usov, N.A. Suvorova, M. Jain, D.M. Feldmann, P.C. Dowden, R.F. Depaula, Q.X. Jia, Rectifying current-voltage characteristics of $BiFeO_3$/Nb-doped $SrTiO_3$ heterojunction, Appl. Phys. Lett. 92 (2008) 102113.